Journal of Computational Physics **161,** 484–511 (2000)
doi:10.1006/jcph.2000.6507, available online at http://www.idealibrary.com on IDEAL®

Divergence Correction Techniques for Maxwell Solvers Based on a Hyperbolic Model

C.-D. Munz,*,† P. Omnes,*,[1] R. Schneider,* E. Sonnendrücker,*,‡ and U. Voß*,§

*Forschungszentrum Karlsruhe—Technik und Umwelt, Institut für Hochleistungsimpuls- und Mikrowellentechnik, Postfach 3640, D-76021 Karlsruhe, Germany; †Institut für Aerodynamik und Gasdynamik, Universität Stuttgart, Pfaffenwaldring 21, D-70550 Stuttgart, Germany; ‡Institut Elie Cartan, Université Henri Poincaré Nancy I, B.P. 239, F-54506 Vandoeuvre les Nancy Cedex, France; §Centre de Mathematiques Appliquées, Ecole Polytechnique, F-91128 Palaiseau Cedex, France

Received March 29, 1999; revised November 16, 1999

Usually, non-stationary numerical calculations in electromagnetics are based on the hyperbolic evolution equations for the electric and magnetic fields and leave Gauss' law out of consideration because the latter is a consequence of the former and of the charge conservation equation in the continuous case. However, in the simulation of the self-consistent movement of charged particles in electromagnetic fields, it is a well-known fact that the approximation of the particle motion introduces numerical errors and that, consequently, the charge conservation equation is not satisfied on the dicrete level. Then, in order to avoid the increase of errors in Gauss' law, a divergence cleaning step which solves a Poisson equation for a correction potential is often added. In the present paper, a new method for incorporating Gauss' law into non-stationary electromagnetic simulation codes is developed, starting from a constrained formulation of the Maxwell equations. The resulting system is hyperbolic, and the divergence errors propagate with the speed of light to the boundary of the computational domain. Furthermore, the basic ideas of the numerical approximation are introduced and the extended hyperbolic system is treated numerically within the framework of high-resolution finite-volume schemes. Simulation results obtained with this new technique for pure electromagnetic wave propagation and for an electromagnetic particle-in-cell computation are presented and compared with other methods.

1. INTRODUCTION

From the beginning of simulating the self-consistent movement of charged particles in electromagnetic fields with particle-in-cell (PIC) methods [3, 13], it has been recognized that

[1] Present address: CEA Saclay—DCC/DPE/SPCP, F-91191 Gif sur Yvette Cedex, France.

0021-9991/00 $35.00

the charge conservation equation may be violated on the discrete level by the approximation procedure itself. As a consequence, unphysical particle orbits may occur [4] resulting in the fact that the solution of the Maxwell–Vlasov model equations runs into unrealistic regimes or may even become unstable. Although the numerical problems are generated by the particle treatment, it is common practice to correct the calculated electrical field from the time-dependent Maxwell equations in order to adjust it to the given charge density [3]. In most cases this is done by deriving, from the divergence constraint established by Gauss' law, a Poisson equation for a correction potential whose gradient improves the electrical field in agreement with the charge density at hand. However, solving this Poisson equation numerically requires much computational effort, the extension to non-regular grid arrangements is difficult, and the parallelization is cumbersome. In order to avoid solving the elliptic Poisson equation, Marder proposed in the field of PIC computations another ansatz resulting in a hyperbolic-parabolic system of equations [24]. Further investigations into this ansatz performed by Nielsen and Drobot [29] and Langdon [19] revealed more detailed insight into its mathematical structure and led to some algorithmic improvements. For a finite-element method Assous *et al.* [2] introduced a constrained formulation of the Maxwell equations and enforced Gauss' law by a penalization technique. Within the finite-element framework the divergence equations may also be taken into account using the least-squares method [16, 17].

In this paper we introduce a new technique to include the divergence constraint due to Gauss' law. For that, we reformulate the so-called constrained formulation of the Maxwell equations by adding a coupling term into Gauss' law that results in a purely hyperbolic model system. The decisive advantage of this approach is that the explicit methods used for the Maxwell equations can be extended to the purely hyperbolic system in a straightforward way, yielding a very efficient and highly flexible Maxwell solver module for PIC applications.

The organization of the present article is as follows. After the introduction of the governing equations and a brief review of the numerical situation in Section 2, different divergence correction techniques are discussed from a general viewpoint in Section 3. Afterwards, in Section 4 the numerical framework for the purely hyperbolic Maxwell system is presented in more detail. In addition, the high-resolution finite-volume (FV) approach for the purely hyperbolic model equations is briefly given, and the numerical approximations are outlined, including the implementation of some relevant physically occurring, as well as computationally motivated, boundary conditions. Section 5 deals with some numerical results obtained from a purely electromagnetic field computation and from a PIC simulation experiment, showing the quality and properties of the applied approximation methods. Finally, conclusive remarks and a short outlook of the further activities are given in Section 6.

2. GOVERNING EQUATIONS

2.1. The Maxwell equations. The evolution of the electromagnetic field is given according to the full set of the Maxwell equations

$$\frac{\partial \boldsymbol{E}}{\partial t} - c^2 \nabla \times \boldsymbol{B} = -\frac{\boldsymbol{j}}{\epsilon_0}, \tag{2.1a}$$

$$\frac{\partial \boldsymbol{B}}{\partial t} + \nabla \times \boldsymbol{E} = 0, \tag{2.1b}$$

$$\nabla \cdot \boldsymbol{E} = \frac{\rho}{\epsilon_0}, \tag{2.1c}$$

$$\nabla \cdot \boldsymbol{B} = 0, \tag{2.1d}$$

where $\boldsymbol{E}$, $\boldsymbol{B}$, ρ, and $\boldsymbol{j}$ denote the electric field, the magnetic induction, the charge, and the current density, respectively. We consider a bounded domain Ω in a homogeneous medium where the permittivity and the magnetic permeability are constant and chosen to be equal to one. The permittivity and permeability of free space ϵ_0 and μ_0, respectively, are related to the speed of light according to $\epsilon_0 \mu_0 c^2 = 1$. The well-known fact that the divergence of the curl of any differentiable vector field is zero leads with (2.1a) and (2.1c) to the charge conservation equation

$$\frac{\partial \rho}{\partial t} + \nabla \cdot \boldsymbol{j} = 0. \tag{2.2}$$

On the other hand, if (2.2) is valid for all times and if the initial data for the electric field and magnetic induction $\boldsymbol{E}_0$ and $\boldsymbol{B}_0$ satisfy (2.1c) and (2.1d), respectively, then the solution of (2.1a) and (2.1b) automatically satisfies Gauss' law (2.1c) and (2.1d) for all times.

2.2. Maxwell equations when charge conservation is not satisfied. Maxwell solvers are usually based on the hyperbolic evolution equations (2.1a) and (2.1b) only, leaving the elliptic part of the Maxwell system (2.1c) and (2.1d) out of consideration. This is motivated by the properties of the exact solution as outlined above. But in the discrete case, there may occur errors of different kinds that substantially disturb the numerical solution and, consequently, generate inconsistencies. Basically, the origin of these errors may be traced back to the used discretization method for the evolution equations (2.1a), (2.1b) and to the applied approximation procedure for the charge and current density, the sources of the Maxwell equations.

While the divergence of the curl of any differentiable vector field is always zero, the discrete approximation may satisfy this fact only approximately. From a more general point of view Hyman and Shashkov [15], Teixeira and Chew [32], and Schwalm *et al.* [30] derive approximations which satisfy discrete analogues of important vector identities. For the Maxwell equations a finite-difference scheme that satisfies the discrete analogue of the *div curl* = 0 relation has been originally proposed by Yee [36]. This approach was extended to curvilinear structured grids by Holland [14] and, furthermore, finite-volume formulations based on the Stokes theorem (see, e.g., [22]) which reduce to the classical Yee scheme in the Cartesian case. All these schemes use a staggered grid arrangement where approximate values of the electromagnetic field components are calculated at different locations within the grid and also at different time levels.

A finite-volume scheme on a collocated grid based on Gauss' theorem has a much simpler data structure than that derived with Stokes' theorem, and robust two-level explicit schemes may be constructed being second or even higher order accurate in both space and time. In this case a discrete analogue of the *div curl* identity does not hold and small approximation errors may appear. In pure field calculations and when the grid is not too distorted this error often seems not to become a severe problem [1, 5, 11, 28].

Another kind of error occurs when the charge conservation equation (2.2) does not hold exactly. This somewhat strange physical situation arises when the Maxwell solver is used as one part of an electromagnetic PIC code with which charged particle simulations in electromagnetic fields are performed in a self-consistent manner [3, 4, 26]. In the PIC framework, the Lorentz force acting on each charge is obtained by interpolating the fields

onto the locations of the particles. Then the new phase space coordinates of the particles are determined by solving numerically the classical Newton–Lorentz equations. Afterwards, charge and current densities are again assigned to the grid points using special location and assignment techniques based on the applied interpolation scheme [3, 13, 25, 34]. These approximation steps introduce numerical errors, and a discrete analogue of the charge conservation equation (2.2) for the Maxwell solvers is not guaranteed to hold exactly. Since only the current density is necessary for the numerical field calculation based on the evolution equations (2.1a) and (2.1b), the consistency of $\nabla \cdot \boldsymbol{E}$ with the charge density ρ may be lost. The consequence of this fact is demonstrated in Fig. 1, where the result of a typical electromagnetic PIC simulation (discussed in more detail below) is depicted.

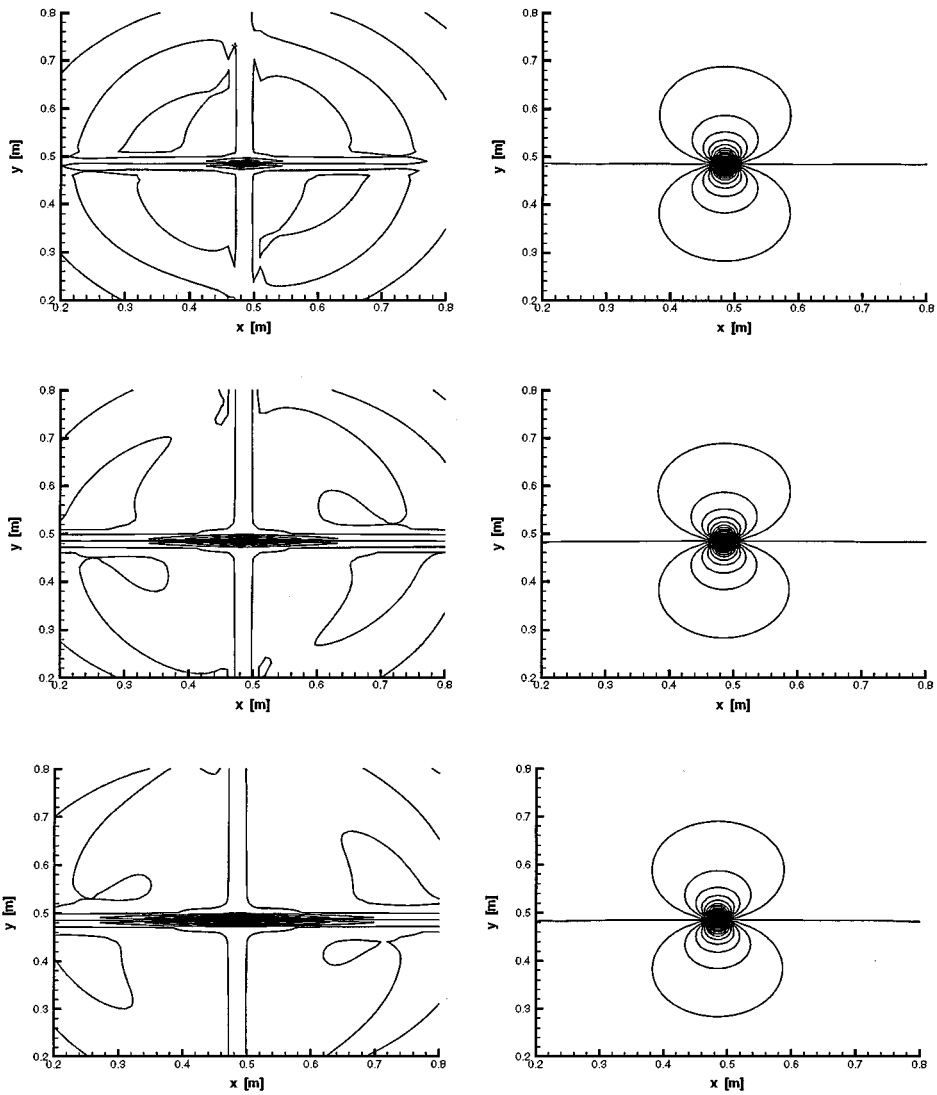

FIG. 1. Temporal evolution of the E_2 field component (1, 3, and 5 ns) obtained from an electromagnetic PIC simulation of a charged particle beam in an external static magnetic field. The numerical errors due to the PIC approximation are not corrected in the sequence of results plotted in the left column while for these depicted in the right column a standard correction approach is applied.

There, snapshots of the temporal evolution (1, 3, and 5 ns) of the E_2 field component of a radiating magnetic dipole are seen for the cases where the numerical error due to local charge conservation violation is not corrected (left column) and where the inconsistency is removed by applying a standard correction technique (right column). Clearly, we recognize from these sequences that it is very important to enforce the divergence constraint (2.1c) in the context of PIC simulations in order to avoid unphysical results as a consequence of not preserving charge conservation numerically. To get rid of this numerical problem, sophisticated particle motion and current density approximations may help to ensure that a discrete analogue of (2.2) is satisfied (see, e.g., [8, 33]). However, a common solution, which we pursue in the present paper, is to enforce the divergence equations (2.1c) and (2.1d) of the Maxwell system by directly incorporating these conditions into the numerical approximations.

In the following, we restrict ourselves to describing the correction of the electric field, because the violation of charge conservation (2.2) influences only that part of the total electromagnetic field. The incorporation of the constraint on the magnetic induction (2.1d) into the numerical algorithm may be done in a similar way.

2.3. The generalized Lagrange multiplier formulation. In the case where the initial data do not satisfy Gauss' law (2.1c), or the charge conservation equation (2.2) is not fulfilled, the divergence constraint (2.1c) has to be coupled with the evolution equation for the electrical field $\boldsymbol{E}$ (2.1a). The standard technique in the context of PIC simulations is to apply first the usual Maxwell solver and compute in a second step a potential whose gradient corrects the electrical field [4]. With respect to the zero charge density case, this correction step is called the projection approach, where the electrical field is projected into a space of divergence-free vector fields. Assous *et al.* [2] formulated this approach by introducing the correction potentials as a Lagrange multiplier into the evolution equation (2.1a) and applied a finite-element method to the set consisting of Eqs. (2.1a), (2.1b), and (2.1c). We generalize the ansatz of Assous *et al.* by defining, for a given linear differential operator $\mathcal{D}(\Phi)$, the set of equations

$$\frac{\partial \boldsymbol{E}}{\partial t} - c^2 \nabla \times \boldsymbol{B} + c^2 \nabla \Phi = -\frac{\boldsymbol{j}}{\epsilon_0}, \tag{2.3a}$$

$$\frac{\partial \boldsymbol{B}}{\partial t} + \nabla \times \boldsymbol{E} = 0, \tag{2.3b}$$

$$\mathcal{D}\Phi + \nabla \cdot \boldsymbol{E} = \frac{\rho}{\epsilon_0}, \tag{2.3c}$$

$$\nabla \cdot \boldsymbol{B} = 0, \tag{2.3d}$$

which we denote as the generalized Lagrange multiplier (GLM) formulation of the Maxwell equations. The new variable Φ introduced into the Maxwell equation (2.1a) defines an additional degree of freedom. Due to the differential operator $\mathcal{D}(\Phi)$ in (2.3c), this variable may be coupled with the divergence condition. For $\mathcal{D}(\Phi) \equiv 0$ the system (2.3) is the constrained formulation of Assous *et al.* [2]. Applying the divergence operator to (2.3a) and differentiating (2.3c) with respect to time yields the following equation for the variable Φ,

$$\frac{\partial \mathcal{D}(\Phi)}{\partial t} - c^2 \nabla^2 \Phi = \frac{1}{\epsilon_0} \left(\frac{\partial \rho}{\partial t} + \nabla \cdot \boldsymbol{j} \right). \tag{2.4}$$

For a given $\boldsymbol{j}$ and ρ, which now must not necessarily satisfy the charge conservation equation (2.2), and for Φ given as a solution of (2.4), it was shown in [27] that the system

(2.3) with appropriate initial and boundary data and under usual regularity conditions admits a unique solution. Moreover, for suitable boundary conditions it can immediately be seen from (2.4) that Φ vanishes when the continuity equation (2.2) is fulfilled. Hence, in this case we get the true solution of the Maxwell equations (2.1). Some other theoretical results are discussed in [27] which guarantee that under the appropriate definition of $\mathcal{D}(\Phi)$ the divergence errors do not increase in time and that (2.1a) and (2.1c) are approximately satisfied. In the present paper we focus our attention on the numerical approximation of the GLM Maxwell system (2.3). For that, the type of the partial differential equation (2.4) for different differential operators $\mathcal{D}(\Phi)$ can be used to classify the different numerical approximation techniques for the system (2.3) discussed in the following sections.

3. DIVERGENCE CORRECTION BASED ON THE REFORMULATED MAXWELL SYSTEM

We now investigate different types of the reformulated Maxwell equations (2.3). For that, we consider here three definitions of the differential operator $\mathcal{D}(\Phi)$ and discuss briefly the essential features of the numerical representation for the resulting formulations.

3.1. The hyperbolic-elliptic approach. The constrained formulation of the Maxwell equations as proposed by [2] is obtained from the GLM Maxwell system (2.3) by taking

$$\mathcal{D}(\Phi) \equiv 0, \tag{3.1a}$$

yielding from (2.4) the Poisson equation

$$-c^2 \nabla^2 \Phi = \frac{1}{\epsilon_0} \left(\frac{\partial \rho}{\partial t} + \nabla \cdot \boldsymbol{j} \right), \tag{3.1b}$$

for the correction potential Φ. The constraint in this case possesses elliptical character and the propagation rate of the correction is infinite. Assuming that $\boldsymbol{E}$ and $\boldsymbol{B}$ satisfy the correct imposed conditions at the boundary, we require homogeneous Dirichlet conditions on Φ,

$$\Phi(\boldsymbol{x}, t) = 0 \qquad \text{for } \boldsymbol{x} \in \partial\Omega \text{ and all } t \geq 0, \tag{3.1c}$$

where $\partial\Omega$ denotes the boundary of the domain Ω.

Let us sketch briefly the numerical scheme. Using a splitting technique for the constrained Maxwell's equations (2.3a), one computes first $\bar{\boldsymbol{E}}^{n+1}$ such that

$$\frac{\bar{\boldsymbol{E}}^{n+1} - \bar{\boldsymbol{E}}^{n}}{\Delta t} - c^2 \tilde{\nabla} \times \boldsymbol{B}^{n+1/2} = \frac{\boldsymbol{j}^{n+1/2}}{\epsilon_0}, \tag{3.2}$$

where $\nabla\Phi$ is approximated implicitly in time, while all other parts are handled by a second-order accurate scheme; then $\boldsymbol{E}^{n+1}$ such that

$$\frac{\boldsymbol{E}^{n+1} - \bar{\boldsymbol{E}}^{n+1}}{\Delta t} + c^2 \tilde{\nabla} \Phi^{n+1} = 0, \tag{3.3}$$

along with

$$\tilde{\nabla} \cdot \boldsymbol{E}^{n+1} = \frac{\rho^{n+1}}{\epsilon_0}, \tag{3.4}$$

which comes from the discretization of (2.3c). The tilde denotes the spatial discretization,

which is not specified more precisely, as the following considerations are valid for different spatial discretization schemes.

Applying the discrete divergence operator $\tilde{\nabla}$ to Eq. (3.3) and substituting the divergence of the electrical field, respectively, according to (3.2) and (3.4), the elliptic equation

$$-c^2\tilde{\nabla}^2\Phi^{n+1} = \frac{1}{\epsilon_0}\left(\frac{\rho^{n+1}-\rho^n}{\Delta t} + \tilde{\nabla}\cdot \boldsymbol{j}^{n+1/2}\right) \tag{3.5}$$

for the potential is obtained, which is obviously the discrete analogue to (3.1b). Hence, this correction can be done in a two-step procedure; first by computing the solution of the usual Maxwell equations (2.1a), (2.1b) and then by adding a correction potential obtained by solving (3.5). This fully implicit approximation with respect to the Lagrange multiplier Φ is identical to the method of Boris [4] and is usually called the projection method. In the correction step the elliptic equation (3.5) together with homogeneous Dirichlet boundary conditions (3.1c) has to be solved, yielding finally the corrected field from (3.3). The main disadvantages of this standard correction approach are that the projection procedure requires a large computational effort and is cumbersome for a straightforward implementation of the numerical scheme on parallel platforms.

We remark that Assous *et al.* [2] solved the constrained formulation within a finite-element framework and incorporated the correction using a penalization.

3.2. The pseudo-current or hyperbolic-parabolic approach. To circumvent the difficulties connected with the implementation of a Poisson solver, Marder [24] added a coupling term to Gauss' law. This Marder ansatz is obtained from the GLM Maxwell system (2.3) choosing the operator $\mathcal{D}(\Phi)$ to be

$$\mathcal{D}(\Phi) = \frac{\Phi}{\chi}, \tag{3.6a}$$

where the quantity χ may be interpreted as a characteristic time scale with seconds as unit. By this choice Eqs. (2.3a) and (2.3c) are artificially coupled with a strength depending on the magnitude of the quantity χ. Clearly, for large values of χ the constrained formulation of Assous *et al.* [2] is obtained. The Marder approach may be called a parabolic ansatz to enforce charge conservation for the following reason. Inserting (3.6a) into (2.4) results in the inhomogeneous parabolic equation

$$\frac{\partial\Phi}{\partial t} - \chi c^2\nabla^2\Phi = \frac{\chi}{\epsilon_0}\left(\frac{\partial\rho}{\partial t} + \nabla\cdot\boldsymbol{j}\right), \tag{3.6b}$$

for the temporal evolution of Φ. Dividing this equation by χ, we recognize immediately that in the limit $\chi\to\infty$ the parabolic approach tends to the elliptic equation (3.1b) for the correction potential. Moreover, the type of (3.6b) reveals something about the mechanism of the correction ansatz, namely, local errors of charge conservation are diffused away by the function Φ. In the case where charge conservation (2.2) is satisfied, the right-hand side of (3.6b) vanishes. This suggests the imposition of

$$\Phi(\boldsymbol{x}, 0) = 0 \qquad \text{for all } \boldsymbol{x}\in\Omega, \tag{3.6c}$$

$$\Phi(\boldsymbol{x}, t) = 0 \qquad \text{for all } \boldsymbol{x}\in\partial\Omega \text{ and } t\geq 0 \tag{3.6d}$$

as initial and boundary conditions on Φ, yielding $\Phi\equiv 0$ in the conservation case.

The starting point for the numerical correction method of $\boldsymbol{E}$ is found by inserting (2.3c) with (3.6a) into (2.3a) yielding

$$\frac{\partial \boldsymbol{E}}{\partial t} - c^2 \nabla \times \boldsymbol{B} = -\frac{\boldsymbol{j}}{\epsilon_0} - \chi c^2 \nabla \left(\frac{\rho}{\epsilon_0} - \nabla \cdot \boldsymbol{E} \right). \tag{3.7}$$

Here, Gauss' law is directly incorporated as an additional current density source term into Maxwell's equation—the reason why the Marder ansatz is also called the pseudo-current approach. For numerical purposes it seems to be reasonable to construct the adequate numerical scheme from (3.7) by applying source term splitting, where the pseudo-current is calculated explicitly. In this process, again the field $\bar{\boldsymbol{E}}^{n+1}$ is computed from Eq. (3.2). Afterwards, this solution is used for the second step in order to compute the corrected electrical field $\boldsymbol{E}^{n+1}$ at $t = t^{n+1}$

$$\boldsymbol{E}^{n+1} = \bar{\boldsymbol{E}}^{n+1} + \chi c^2 \tilde{\nabla} \left(\frac{\rho^n}{\epsilon_0} - \tilde{\nabla} \cdot \bar{\boldsymbol{E}}^{n+1} \right) \tag{3.8}$$

for Marder's approached Maxwell formulation. Originally, in the scheme given by Marder the computations are performed the other way round. As a first improvement, the sequence (3.2), (3.8) has been proposed by Nielsen and Drobot [29] and Langdon [19]. Langdon pointed out in his article that these two steps can also be regarded as the first iteration sweep in solving the Poisson equation with a Jacobi iteration scheme. Nielsen and Drobot reported in [29] that a large number of repeated iterations of (3.8) would asymptotically converge to the solution of Poisson's equation (3.1b), whereas in practice a few iterations are sufficient.

3.3. The purely hyperbolic formulation. The new, strictly hyperbolic correction approach may be deduced from the GLM equations (2.3) choosing $\mathcal{D}(\Phi)$ as

$$\mathcal{D}(\Phi) = \frac{1}{\chi^2} \frac{\partial \Phi}{\partial t}, \tag{3.9a}$$

where the—now—dimensionless parameter χ determines the strength of the artificial coupling between (2.3a) and (2.3c). The temporal evolution of the defect Φ is given by inserting (3.9a) into (2.4), yielding the inhomogeneous wave equation

$$\frac{\partial^2 \Phi}{\partial t^2} - (\chi c)^2 \nabla^2 \Phi = \frac{\chi^2}{\epsilon_0} \left(\frac{\partial \rho}{\partial t} + \nabla \cdot \boldsymbol{j} \right), \tag{3.9b}$$

which is a hyperbolic partial differential equation, transporting information with the finite propagation velocity χc out of the computational domain. As pointed out in [27] this defect may also be interpreted as a general gauge condition and, hence, (3.9b) propagates simply the resulting gauge error. Note that the purely hyperbolic formulation is the only model system which is fully relativistic. Dividing (3.9b) by χ^2 yields that this hyperbolic equation formally converges to the elliptic equation (3.1b) for the correction potential in the limit $\chi \to \infty$ and, consequently, establishes the hyperbolic-elliptic formulation. The size of the parameter χ is yet unknown and has to be estimated from numerical experiments. However, the fact that the defect Φ should be transported at least as fast as the electromagnetic fields propagate results in the a priori choice $\chi \geq 1$. Since the right-hand side of (3.9b) vanishes if the charge conservation equation (2.2) holds, we require the initial conditions

$$\Phi(\boldsymbol{x}, 0) = 0 \qquad \text{for all } \boldsymbol{x} \in \Omega \tag{3.9c}$$

for Φ, ensuring $\Phi \equiv 0$ in that case. In order to guarantee that the hyperbolic formulation (2.3) with (3.9a) satisfies the Maxwell equations (2.1) approximately for all times in the bounded domain Ω, we have to impose additionally the radiation condition

$$\frac{\partial \Phi}{\partial t} + \chi c \frac{\partial \Phi}{\partial \zeta} = 0 \qquad \text{for all } \boldsymbol{x} \in \partial\Omega, \tag{3.9d}$$

at the boundary $\partial\Omega$ on Φ, where $\frac{\partial \Phi}{\partial \zeta} = \boldsymbol{n} \cdot \nabla \Phi$ denotes the normal derivative at the border. Such a boundary condition provides a stabilization of the wave equation (3.9b) at the truncated domain. Further boundary conditions stabilizing the wave equation at the border can be considered and are discussed, for instance, in [18]. Under the assumption that $\| \frac{\partial \Phi}{\partial t} \|$ is bounded on a finite time interval, the convergence of the purely hyperbolic solution towards the hyperbolic-elliptic solution can be proved [27].

To construct a finite-volume scheme, we rewrite Eqs. (2.3a), (2.3b), and (2.3c) with (3.9a) as a system of linear hyperbolic evolution equations

$$\frac{\partial \boldsymbol{w}}{\partial t} + \sum_{j=1}^{D} \frac{\partial}{\partial x_j} (\mathcal{A}_j \boldsymbol{w}) = \boldsymbol{s}, \tag{3.10a}$$

where we restrict ourselves in the present description to two dimensions ($D = 2$) in space. The vector of the unknown quantities $\boldsymbol{w} = \boldsymbol{w}(\boldsymbol{x}, t)$ is given by

$$\boldsymbol{w} = (E_1, E_2, E_3, B_1, B_2, B_3, \Phi)^T. \tag{3.10b}$$

The 7×7 matrices $\mathcal{A}_j$ with constant entries are defined as

$$\mathcal{A}_j = \begin{pmatrix} 0 & 0 & 0 & & & & c^2\delta_{1j} \\ 0 & 0 & 0 & & c^2\mathcal{M}_j & & c^2\delta_{2j} \\ 0 & 0 & 0 & & & & 0 \\ & & & 0 & 0 & 0 & 0 \\ & \mathcal{M}_j^T & & 0 & 0 & 0 & 0 \\ & & & 0 & 0 & 0 & 0 \\ \chi^2\delta_{1j} & \chi^2\delta_{2j} & 0 & 0 & 0 & 0 & 0 \end{pmatrix}; \qquad j = 1, 2, \tag{3.10c}$$

where δ_{ij} denotes the usual Kronecker symbol and the two 3×3 matrices $\mathcal{M}_j$ are found to be

$$\mathcal{M}_1 = \begin{pmatrix} 0 & 0 & 0 \\ 0 & 0 & 1 \\ 0 & -1 & 0 \end{pmatrix}, \qquad \mathcal{M}_2 = \begin{pmatrix} 0 & 0 & -1 \\ 0 & 0 & 0 \\ 1 & 0 & 0 \end{pmatrix}. \tag{3.10d}$$

The right-hand side of (3.10a) contains the current as well as the charge density and reads as

$$\boldsymbol{s} = -\frac{1}{\epsilon_0} (j_1, j_2, j_3, 0, 0, 0, -\chi^2 \rho)^T. \tag{3.10e}$$

For further discussion, the properties of the linear combination of the matrices $\mathcal{A}_j$

$$\mathbb{A} = \sum_{j=1}^{D} n_j \mathcal{A}_j, \qquad \text{with } \sum_{j=1}^{D} n_j^2 = 1, \tag{3.11a}$$

are important. In summary, we notice that the matrix $\mathbb{A} \in \mathbb{R}^{7\times 7}$ possesses seven real eigenvalues λ_i

$$\Lambda = \operatorname{diag}(\lambda_1, \ldots, \lambda_7) = \operatorname{diag}(-\chi c, -c, -c, 0, c, c, \chi c), \tag{3.11b}$$

and a complete set of right eigenvectors $\mathcal{R} = (\boldsymbol{r}_1, \ldots, \boldsymbol{r}_7)$,

$$\mathcal{R} = \begin{pmatrix} -n_1\frac{c}{\chi} & n_2 c & 0 & 0 & -n_2 c & 0 & n_1\frac{c}{\chi} \\ -n_2\frac{c}{\chi} & -n_1 c & 0 & 0 & n_1 c & 0 & n_2\frac{c}{\chi} \\ 0 & 0 & -\frac{c}{n_2} & 0 & 0 & \frac{c}{n_2} & 0 \\ 0 & 0 & 1 & 1 & 0 & 1 & 0 \\ 0 & 0 & -\frac{n_1}{n_2} & \frac{n_2}{n_1} & 0 & -\frac{n_1}{n_2} & 0 \\ 0 & 1 & 0 & 0 & 1 & 0 & 0 \\ 1 & 0 & 0 & 0 & 0 & 0 & 1 \end{pmatrix}. \tag{3.11c}$$

Hence, the considered extended Maxwell system is strictly hyperbolic.

4. NUMERICAL FRAMEWORK FOR THE HYPERBOLIC MAXWELL SYSTEM

In the following section we propose a finite-volume (FV) scheme on a collocated grid for the hyperbolic formulation introduced in the previous section.

4.1. Presentation of the numerical scheme. The domain of computation $\Omega = \bigcup_{i=1}^{N} C_i$ is covered by a set of N non-overlapping grid zones C_i. The border ∂C_i of each grid zone C_i consists of σ_i edges $S_{i,\beta}$ with length $L_{i,\beta}$, where β runs from one to σ_i (for example, $\sigma_i = 3$ for triangles and $\sigma_i = 4$ for quadrilaterals). The solution is computed at a set of discrete $t^n = n\Delta t$, where Δt is determined with respect to the CFL condition. Integrating each component of the evolution system (3.10a) over the space-time volume $C_i \times [t^n, t^{n+1}]$ and applying Gauss' theorem to the integral of the divergence of the flux components, we obtain the exact evolution equation

$$V_i\left[\boldsymbol{w}_i^{n+1} - \boldsymbol{w}_i^n\right] = -\sum_{\beta=1}^{\sigma_i} \int_{t^n}^{t^{n+1}} \int_{S_{i,\beta}} \left[\sum_{j=1}^{D} (n_j)_{i,\beta} \mathcal{A}_j\right] \boldsymbol{w}(\boldsymbol{x}, t)\, dS\, dt + \int_{t^n}^{t^{n+1}} \int_{C_i} \boldsymbol{s}\, dV\, dt, \tag{4.1a}$$

where we replaced the line integral over the border by the sum of integrals over the edges of C_i. Here, $\boldsymbol{w}_i^n$ is the cell average of $\boldsymbol{w}$ over the cell C_i with the area V_i at time $t = t^n$ given by

$$\boldsymbol{w}_i^n = \frac{1}{V_i} \int_{C_i} \boldsymbol{w}(\boldsymbol{x}, t^n)\, dV, \tag{4.1b}$$

and $(n_j)_{i,\beta}$ denotes the jth component of the outwards directed unit normal $\boldsymbol{n}_{i,\beta}$ at the edge $S_{i,\beta}$. The direct approximation of the integral formulation (4.1a) yields the FV scheme, usually written in the form

$$\boldsymbol{w}_i^{n+1} = \boldsymbol{w}_i^n - \frac{\Delta t}{V_i} \sum_{\beta=1}^{\sigma_i} \boldsymbol{G}_{i,\beta}^n + \Delta t\, \boldsymbol{s}_i^n. \tag{4.2a}$$

The scheme is completely defined if the numerical flux $\boldsymbol{G}_{i,\beta}^n$ is specified as a suitable approximation of the physical flux through the boundary edge $S_{i,\beta}$, which means

$$\boldsymbol{G}_{i,\beta}^n \approx \frac{1}{\Delta t} \int_{t^n}^{t^{n+1}} \int_{S_{i,\beta}} \mathbb{A}_{i,\beta} \boldsymbol{w}(\boldsymbol{x}, t)\, dS\, dt, \tag{4.2b}$$

where $\mathbb{A}_{i,\beta}$ is defined according to (3.11a). The vector $\boldsymbol{s}_i^n$ approximates the source term (3.10e) averaged over V_i and the time interval $\Delta t = t^{n+1} - t^n$. The main task in the context of FV schemes is to find a suitable numerical flux (4.2b) as a function of the averaged quantities (4.1b). Moreover, as indicated by the superscript n of the numerical flux in (4.2a), we are interested in an explicit approximation of the fluxes using only the values at the previous time level $t = t^n$.

4.2. Calculation of the numerical flux. In this section we outline the path of approximations to obtain the numerical flux $\boldsymbol{G}_{i,\beta}^n$. In order to do that, we apply the second-order midpoint rule to the integral (4.2b), yielding the first approximation

$$\boldsymbol{G}_{i,\beta}^n = L_{i,\beta} \mathbb{A}_{i,\beta} \boldsymbol{w}(M_{i,\beta}, t^n), \tag{4.3}$$

where $M_{i,\beta}$ denotes the midpoint of the edge $S_{i,\beta}$. An approximation of the solution at that midpoint is calculated by applying the method of Godunov [10] (for a review of these methods we refer to [21]). For the following, we assume that the approximated solution is constant in each grid zone and given according to the integral values (4.1b) at the time level $t = t^n$. Information about the break-up of the jump into propagating waves at the grid zone interface $S_{i,\beta}$ at $M_{i,\beta}$ is provided by analyzing the local wave structure. This can be performed by solving a Riemann problem (RP) at $M_{i,\beta}$ into the direction of the normal $\boldsymbol{n}_{i,\beta}$ (cf. Fig. 2). The RP at the time level $t = t^n$ is an initial-value problem of the form

$$\frac{\partial \boldsymbol{w}}{\partial t} + \mathbb{A} \frac{\partial \boldsymbol{w}}{\partial \zeta} = 0; \qquad \boldsymbol{w}(\zeta, 0) = \begin{cases} \boldsymbol{w}_i^n & \text{for } \zeta < 0 \\ \boldsymbol{w}_{i_\beta}^n & \text{for } \zeta > 0, \end{cases} \tag{4.4}$$

where the coordinate ζ is associated with the normal $\boldsymbol{n}_{i,\beta}$, and $\boldsymbol{w}_i^n$ and $\boldsymbol{w}_{i_\beta}^n$ denote the initial data in the grid zone C_i and its neighbor cell C_{i_β}, respectively. The solution of the RP for the linear Maxwell equations is found by applying the theory of characteristics, for instance, explicitly performed in [9, 28]. The exact solution of this initial-value problem in the (ζ, t)-plane for the approached hyperbolic Maxwell model is schematically depicted in Fig. 2. The characteristics associated with the eigenvalues of $\mathbb{A}_{i,\beta}$ (cf. (3.11b)) separate six constant states $\boldsymbol{w}_0, \boldsymbol{w}_1, \ldots, \boldsymbol{w}_5$, where $\boldsymbol{w}_0 = \boldsymbol{w}_i^n$ and $\boldsymbol{w}_5 = \boldsymbol{w}_{i_\beta}^n$ are the initial data of the RP. Replacing in (4.3) the term $\boldsymbol{w}(M_{i,\beta}, t^n)$ by the solution of the RP, the numerical flux of the

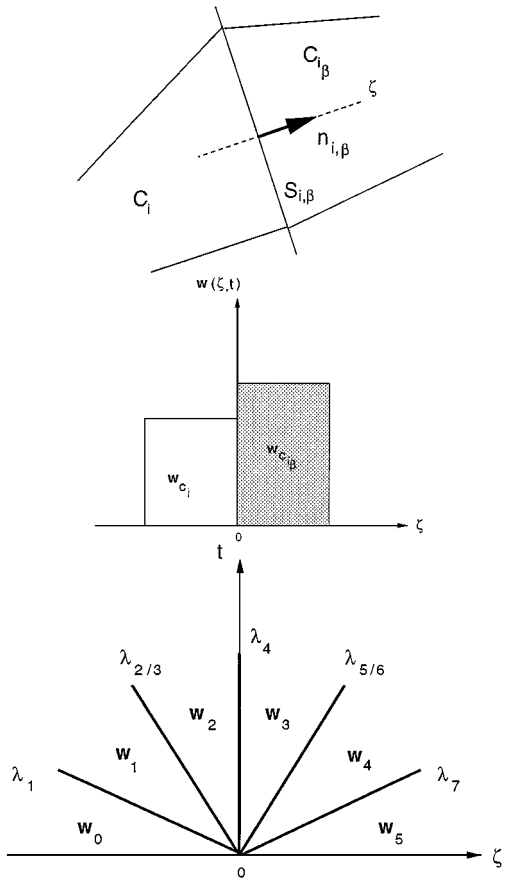

FIG. 2. Schematic solution of the Riemann problem in the direction of the normal $\boldsymbol{n}_{i,\beta}$ at the interface $S_{i,\beta}$ between the grid zones C_i and C_{i_β}.

Godunov scheme is finally obtained and can be written as

$$\boldsymbol{G}^n_{i,\beta} = L_{i,\beta}\left(\mathbb{A}^+_{i,\beta}\boldsymbol{w}^n_i + \mathbb{A}^-_{i,\beta}\boldsymbol{w}^n_{i_\beta}\right), \tag{4.5a}$$

where the matrices $\mathbb{A}^\pm_{i,\beta}$ are decomposed for later purposes according to

$$\mathbb{A}^\pm_{i,\beta} = \mathbb{K}^\pm_{i,\beta} + \mathbb{H}^\pm_{i,\beta}. \tag{4.5b}$$

Explicitly, these 7×7 matrices $\mathbb{K}^\pm_{i,\beta}$ and $\mathbb{H}^\pm_{i,\beta}$ are given by

$$\mathbb{K}^\pm_{i,\beta} = \frac{1}{2}\begin{pmatrix} \pm b^2c & \mp abc & 0 & 0 & 0 & -bc^2 & 0 \\ \mp abc & \pm a^2c & 0 & 0 & 0 & ac^2 & 0 \\ 0 & 0 & \pm c & bc^2 & -ac^2 & 0 & 0 \\ 0 & 0 & b & \pm b^2c & \mp abc & 0 & 0 \\ 0 & 0 & -a & \mp abc & \pm a^2c & 0 & 0 \\ -b & a & 0 & 0 & 0 & \pm c & 0 \\ 0 & 0 & 0 & 0 & 0 & 0 & 0 \end{pmatrix}, \tag{4.5c}$$

and

$$\mathbb{H}^{\pm}_{i,\beta} = \frac{1}{2}\begin{pmatrix} \pm a^2\chi c & \pm ab\chi c & 0 & 0 & 0 & 0 & ac^2 \\ \pm ab\chi c & \pm b^2\chi c & 0 & 0 & 0 & 0 & bc^2 \\ 0 & 0 & 0 & 0 & 0 & 0 & 0 \\ 0 & 0 & 0 & 0 & 0 & 0 & 0 \\ 0 & 0 & 0 & 0 & 0 & 0 & 0 \\ 0 & 0 & 0 & 0 & 0 & 0 & 0 \\ a\chi^2 & b\chi^2 & 0 & 0 & 0 & 0 & \pm\chi c \end{pmatrix}, \tag{4.5d}$$

where the abbreviations $a = (n_1)_{i,\beta}$ and $b = (n_2)_{i,\beta}$ are used. The flux-vector splitting formulation (4.5a) of the total numerical flux $\boldsymbol{G}^n_{i,\beta}$ is a decomposition into a flux to the "right" having positive eigenvalues only, and into a flux to the "left" having negative eigenvalues only associated with $\mathbb{A}^+_{i,\beta}$ and $\mathbb{A}^-_{i,\beta}$ respectively. Obviously from (4.5a), the first matrix acts on the left while the second one acts on the right initial state of the RP (cf. Fig. 2), honoring in that way the correct range of influence. These considerations are valid only if the time step size is short enough to guarantee that the waves generated at different grid zone interfaces do not interact. This leads to the CFL time step restriction in the form $\chi c \frac{\Delta t}{h} \leq 1$, where h denotes the smallest grid zone length. For Cartesian grids the FV scheme presented above agrees with the Courant–Isaacson–Rees scheme [6], which is based on the characteristic form of the equations. However, the Godunov approximation technique with the flux-vector splitting formulation may be considered as an extension of this scheme to general mesh arrangements. Because the direction of the wave propagation is directly taken into account, this numerical method is inherently very robust and able to resolve steep gradients without generating spurious oscillations. But in the described form, the Godunov scheme is only first-order accurate in both space and time and introduces too much numerical dissipation for practical calculations. This lack can be removed by an extension of the scheme to higher-order accuracy as proposed by van Leer in his MUSCL approach [20]: Instead of a piecewise constant, a piecewise linear reconstruction from the average values (4.1b) is used. These improved approximations are then used to compute the new, now second-order accurate numerical flux via the RP. For a more comprehensive discussion of accuracy improvement we refer to [7, 21, 28].

4.3. Splitting approach. Another technique to solve the equations with the hyperbolic correction is to apply a splitting scheme [23]. In order to do this, we consider the matrices $\mathcal{A}_j \in \mathbb{R}^{7\times 7}$ (3.10c) and recognize that they can split up into a sum of two matrices

$$\mathcal{A}_j = \mathcal{K}_j + \mathcal{H}_j; \qquad j = 1, 2, \tag{4.6a}$$

where the entries of the last column and row of the $\mathcal{A}_j$ are shifted to the $\mathcal{H}_j$ while the corresponding column and row of the $\mathcal{K}_j$ are set equal to zero. A similar procedure of decomposition can be performed for the source $\boldsymbol{s}$ (3.10e) resulting in

$$\begin{aligned} \boldsymbol{s} &= \boldsymbol{q} + \boldsymbol{g} \\ &= -\frac{1}{\epsilon_0}(j_1, j_2, j_3, 0, 0, 0, 0)^T + \frac{1}{\epsilon_0}(0, 0, 0, 0, 0, 0, \chi^2\rho)^T. \end{aligned} \tag{4.6b}$$

Obviously, this procedure transfers to the evolution equation (3.10a), leading to a decomposition in the suggestive form

$$\frac{\partial \boldsymbol{w}}{\partial t} + \sum_{j=1}^{D} \frac{\partial}{\partial x_j}(\mathcal{K}_j \boldsymbol{w}) - \boldsymbol{q} = \boldsymbol{g} - \sum_{j=1}^{D} \frac{\partial}{\partial x_j}(\mathcal{H}_j \boldsymbol{w}). \tag{4.6c}$$

Here, the left-hand side represents nothing else than the Maxwell equations (2.1a) and (2.1b), being the starting point for an uncorrected FV-based Maxwell solver. At each time step, first the solver provides the solution of the uncorrected Maxwell equations (2.1a) and (2.1b) in the time domain

$$\bar{\boldsymbol{w}}(\boldsymbol{x}, t_*) = \boldsymbol{w}(\boldsymbol{x}, t^n) - \Delta t\, \mathcal{L}_{UC}(\boldsymbol{w}(\boldsymbol{x}, t^n)), \tag{4.7a}$$

where $\boldsymbol{w}(\boldsymbol{x}, t^n)$ denotes the charge corrected numerical solution of the previous temporal iteration cycle and $\mathcal{L}_{UC}$ is the spatial approximation of $\sum_{j=1}^{D}(\partial/\partial x_j)[\mathcal{K}_j \boldsymbol{w}(\boldsymbol{x}, t^n)] - \boldsymbol{q}$. Afterwards, the correction is performed according to

$$\begin{aligned} &\boldsymbol{w}(\boldsymbol{x}, t^n + (k+1)\Delta t) \\ &\quad = \boldsymbol{w}(\boldsymbol{x}, t^n + k\Delta t) - \Delta t \mathcal{L}_{HC}(\boldsymbol{w}(\boldsymbol{x}, t^n + k\Delta t)), \qquad k = 0, \ldots, \chi - 1, \end{aligned} \tag{4.7b}$$

where $\mathcal{L}_{HC}$ denotes the spatial discretization of the operator $\sum_{j=1}^{D}(\partial/\partial x_j)[\mathcal{H}_j \boldsymbol{w}(\boldsymbol{x}, t^n + k\Delta t)] - \boldsymbol{g}$. Definitively, this procedure has at least two advantages. First, and kind of Maxwell solver may be used for the solution of the uncorrected system, followed by an independent charge conservation correction computation. We remark that for this correction step, approximations other than our FV approach may be applied. The second advantage concerns the choice of the free parameter χ. This quantity may be chosen in a way that the corresponding correction propagation is larger than the speed of light, which would affect the time step size due to the CFL condition. However, performing the charge correction by the proposed splitting approach, the stronger CFL restriction for the Maxwell solver could be avoided by a sub-cycling technique for the correction computation choosing a smaller time step size $\Delta\tau$ and iterating the correction part several times.

From the structure of the matrices $\mathcal{H}_j$ or $\mathcal{A}_j$ it is obvious that in two space dimensions only the electrical field components E_1, E_2 and the potential Φ enter into the hyperbolic correction scheme. Additionally, we remark that the operators $\mathcal{K}_i(\partial/\partial x_i)$ and $\mathcal{H}_j(\partial/\partial x_j)$ commute for all $i, j = 1, 2$ and, hence, no Strang splitting [31] is necessary to preserve the order of the considered numerical scheme with respect to time.

4.4. Implementation of boundary conditions. As already mentioned, we restrict ourselves in the present paper to two spatial dimensions and describe boundary conditions for the transverse electric (TE) field components. This means, besides the boundary conditions for the correction Φ, we have to investigate the boundary conditions for the field components E_1, E_2, and B_3 more closely. Three-dimensional conditions can be obtained in a straightforward way.

In general, boundary conditions and their implementation for hyperbolic systems are well-posed if the wave propagation as given by the theory of characteristics is locally taken into account. This may be established if the solution of initial-boundary-value problems for grid zones adjacent to the border of the computational domain is incorporated. It is possible

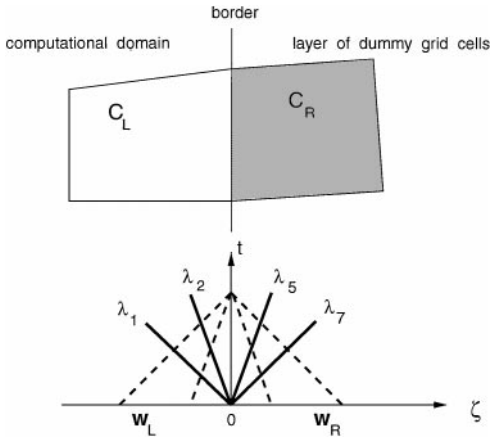

FIG. 3. The value in the dummy cell C_R adjacent to the border grid zone C_L is specified in such a way that the solution of the Riemann problem at the border $\zeta = 0$ (lower picture) yields the imposed boundary condition.

to reformulate these initial-boundary-value problems as Riemann problems, fitting more properly in the numerical framework of FV methods. In order to do this, first dummy grid cells are introduced, surrounding the domain of computation (cf. Fig. 3). Then in these mesh zones, values for the dependent variables are prescribed in such a way that the solution of the RP at the border yields the physically imposed or computationally motivated boundary conditions. The main advantage of such a procedure is that imposing boundary conditions is equivalent to specifying appropriate values for the dummy cells which can be managed in the first step of the computation cycle. In the second sweep, the discrete equations can be solved without any further modification in the computational domain, leading to a highly vectorizable algorithm. In the context of parallel code running, this technique seems also to be very attractive since data exchange of boundary values is necessary if domain decomposition strategies are applied.

More precisely, to obtain the solution of the RP at the border of the computational domain $\zeta = 0$ (cf. Fig. 3), we apply the theory of characteristics and define the characteristic variables $\boldsymbol{v}$ according to

$$\boldsymbol{v}(\zeta, t) = \mathcal{R}^{-1}\boldsymbol{w}(\zeta, t), \tag{4.8a}$$

where $\mathcal{R}^{-1}$ is the inverse matrix of (3.11c). With this transformation the RP (4.4) can be recast into a set of seven uncoupled linear transport equations whose solutions are given by

$$v_k(\zeta, t) = v_k^{(0)}(\zeta - \lambda_k t); \qquad k = 1, \ldots, 7, \tag{4.8b}$$

with the initial values $\boldsymbol{v}^{(0)} = \mathcal{R}^{-1}\boldsymbol{w}(\zeta, 0)$ and the propagation velocities λ_k defined by (3.11b). For the problem of interest, the relevant characteristic variables are schematically depicted in Fig. 3 and explicitly calculated from (4.8a) at the border $\zeta = 0$ according to

$$v_{1,R} = v_1^{(0)}(\chi ct) = \frac{\chi}{2c}\left[-aE_{1,R} - bE_{2,R} + \frac{c}{\chi}\Phi_R\right], \tag{4.9a}$$

$$v_{2,R} = v_2^{(0)}(ct) = \frac{1}{2c}[bE_{1,R} - aE_{2,R} + cB_{3,R}], \tag{4.9b}$$

$$v_{5,L} = v_5^{(0)}(-ct) = \frac{1}{2c}[-bE_{1,L} + aE_{2,L} + cB_{3,L}], \tag{4.9c}$$

$$v_{7,L} = v_7^{(0)}(-\chi ct) = \frac{\chi}{2c}\left[aE_{1,L} + bE_{2,L} + \frac{c}{\chi}\Phi_L\right]. \tag{4.9d}$$

Here, the subscript R indicates that information is propagated from the dummy cell C_R to the border by the characteristic variables v_1 and v_2 with the velocity $\lambda_1 = -\chi c$ and $\lambda_2 = -c$, respectively. The other way round, namely, the information transport by v_5 and v_7 from the border grid zone C_L to the boundary of the domain with the speed $\lambda_5 = c$ and $\lambda_7 = \chi c$, is abbreviated by the subscript L. It is obvious that the latter two characteristic variables are always determined by a condition of compatibility while $v_{1,R}$ and $v_{2,R}$ are unknown and, consequently, have to be fixed in an appropriate manner. In terms of the characteristic variables (4.4), the solution of the RP at the boundary of the computational domain $\boldsymbol{w}_0 = \boldsymbol{w}(0, t)$ reads as

$$w_{1,0} = E_{1,0} = a\frac{c}{\chi}[-v_{1,R} + v_{7,L}] + bc[v_{2,R} - v_{5,L}], \tag{4.10a}$$

$$w_{2,0} = E_{2,0} = b\frac{c}{\chi}[-v_{1,R} + v_{7,L}] + ac[-v_{2,R} + v_{5,L}], \tag{4.10b}$$

$$w_{5,0} = B_{3,0} = v_{2,R} + v_{5,L}, \tag{4.10c}$$

$$w_{7,0} = \Phi_0 = v_{1,R} + v_{7,L}, \tag{4.10d}$$

where the characteristics $v_{1,R}$ and $v_{2,R}$ are the variables which have to be calculated at the boundary. This RP solution is completely determined if these unknown incoming characteristic variables are specified. In the following we describe how to specify these two characteristics for some relevant physically occurring as well as computationally motivated boundary conditions.

4.4.1. Perfect conducting wall. The boundary condition of a perfect conducting wall, where the fields cannot penetrate into the surface, reads as

$$\boldsymbol{n} \times \boldsymbol{E}_0 = 0, \qquad \boldsymbol{n} \cdot \boldsymbol{B}_0 = 0. \tag{4.11a}$$

These conditions lead to

$$aE_{2,0} - bE_{1,0} = 0, \qquad B_{3,0} \text{ is undefined} \tag{4.11b}$$

for the TE field components at the border $\zeta = 0$. With (4.10a) and (4.10b), the first condition yields that the incoming characteristic $v_{2,R}$ is determined by $v_{2,R} = v_{5,L}$, resulting in the possible covering

$$E_{1,R} = -E_{1,L}, \qquad E_{2,R} = -E_{2,L}, \qquad B_{3,R} = B_{3,L} \tag{4.11c}$$

of the dummy grid zones C_R for the electromagnetic fields. The other incoming characteristic $v_{1,R}$ and, by that, a possible choice of the correction Φ_R in the dummy cells have to be calculated from (4.10d) by prescribing the value Φ_0 of the correction at the boundary $\zeta = 0$ in a suitable manner. In order to be more flexible for further investigations, we will consider

in the present context the discretization of the more general radiation condition

$$\frac{\partial \Phi}{\partial t} + \chi c \frac{\partial \Phi}{\partial \zeta} + \nu \Phi = 0 \qquad \text{with } \nu \geq 0, \tag{4.12}$$

for the correction Φ at the border. Clearly, this extended condition provides the radiation condition (3.9d) at the border $\zeta = 0$ if ν is fixed to zero. Choosing for the further considerations a new function $\tilde{\Phi}$ defined by the ansatz

$$\tilde{\Phi}(\zeta, t) = \Phi(\zeta, t) e^{\nu t}, \tag{4.13a}$$

the radiation condition (4.12) may be recast into an equivalent linear transport equation

$$\frac{\partial \tilde{\Phi}}{\partial t} + \chi c \frac{\partial \tilde{\Phi}}{\partial \zeta} = 0, \tag{4.13b}$$

at the border $\zeta = 0$, having the solution $\tilde{\Phi}(\zeta, t) = \tilde{\Phi}^{(0)}(\zeta - \chi c t)$. As a consequence of compatibility we assume that the border state Φ_L located inside the computational domain is transported within the time step size Δt to the border. Hence, at the boundary $\zeta = 0$ we have $\tilde{\Phi}(0, \Delta t) = \tilde{\Phi}(-\chi c \Delta t) = \Phi_L$, resulting with (4.13a) in

$$\Phi_0 = \Phi(0, \Delta t) = \Phi_L \mathrm{e}^{-\nu \Delta t}, \tag{4.14}$$

which is a possible approximation of the value of the correction at the border. Inserting the last relation into (4.10d) and performing some rearrangements using (4.9a) and (4.9d), we obtain

$$\Phi_R = \alpha \Phi_L - 2 \frac{\chi}{c} [a E_{1,L} + b E_{2,L}] \tag{4.15a}$$

with

$$\alpha = 2\mathrm{e}^{-\nu \Delta t} - 1 \tag{4.15b}$$

for the covering of the dummy grid zones C_R, where the prescriptions (4.11c) for the electromagnetic fields are used. Immediately from (4.14), two limit cases may be deduced: First, for the choice $\nu = 0$ ($\alpha = 1$) we obtain the "transmission case" $\Phi_0 = \Phi_L$ which is a direct result of the radiation condition (3.9d) at the boundary. Second, the "reflecting case" is established by setting ν equal to $\nu = +\infty$ ($\alpha = -1$). Obviously, this reflection case leads to strong attenuation, resulting in the fact that Φ_0 vanishes at the border of the computational domain. It is judicious that the choices $0 < \nu < \infty$ may be interpreted as compromises between the two limit cases and denoted as the "mixed radiation case" for the correction function Φ at the boundary of the domain.

4.4.2. Irradiation condition. We denote by irradiation the process where energy in the form of electromagnetic waves is irradiated at certain scheduled edges of the domain into the computational domain. Again, we restrict our discussion to the TE system and assume that the incoming electromagnetic fields denoted by $\epsilon_1(\boldsymbol{x}, t)$, $\epsilon_2(\boldsymbol{x}, t)$, and $\beta_3(\boldsymbol{x}, t)$ are known at the border $\zeta = 0$,

$$E_{1,0} = \epsilon_1(0, t), \qquad E_{2,0} = \epsilon_2(0, t), \qquad B_{3,0} = \beta_3(0, t), \tag{4.16a}$$

determining the incoming characteristic variable as

$$v_{2,0} = \frac{1}{2c} [b\epsilon_1 - a\epsilon_2 + c\beta_3]. \tag{4.16b}$$

However, we notice from Eq. (4.10c) that only two of the three components (4.16a) of the TE subsystem at $\zeta = 0$ are important to know. For instance, if $E_{1,0}$ and $E_{2,0}$ are given, the magnetic induction at the border can immediately be computed as

$$\begin{aligned} B_{3,0} &= v_{2,R} + v_{5,L} \\ &= \frac{1}{c}[b(E_{1,0} - E_{1,L}) - a(E_{2,0} - E_{2,L}) + cB_{3,L}], \end{aligned} \tag{4.16c}$$

depending on values specified at $\zeta = 0$ and on those coming from the interior of the computational domain. Using (4.9b) and (4.9c) in the explicit form, we further obtain from the last relation the following covering of the dummy grid zones C_R

$$E_{1,R} = 2E_{1,0} - E_{1,L}, \qquad E_{2,R} = 2E_{2,0} - E_{2,L}, \qquad B_{3,R} = B_{3,L} \tag{4.17a}$$

for the electromagnetic fields to meet the imposed boundary condition at $\zeta = 0$. In order to specify the correction Φ in the dummy cells C_R, we assume that the value Φ_0 at the boundary is given, for instance by (4.14). Then, applying Eq. (4.10d) we calculate for the covering of the ghost cells C_R the values

$$\Phi_R = 2\Phi_0 - \Phi_L + 2\frac{\chi}{c}[a(E_{1,0} - E_{1,L}) + b(E_{2,0} - E_{2,L})], \tag{4.17b}$$

for the correction, where the result obtained for the TE fields (4.17a) is taken into account.

4.4.3. Truncated domain condition. Comprehensive numerical simulations often require an artificial limit to the computational domain. This computationally motivated truncation is realized by introducing "open boundary conditions." A sensible characterization of open boundaries has been formulated by Hedstrom [12]: No wave coming from outside should propagate into the computational domain which is synonymous with the fact that the amplitudes of incoming waves are constant with respect to time at the border $\zeta = 0$. Hence, the TE field components at the boundary are completely specified by the outgoing traveling waves associated with the characteristics v_5 and v_7 possessing positive eigenvalues. Consequently, compatibility reasons ensure that the TE system at $\zeta = 0$ is imposed by the v_5 variable according to

$$E_{1,0} = E_{1,L}, \qquad E_{2,0} = E_{2,L}, \qquad B_{3,0} = B_{3,L}. \tag{4.18}$$

At this stage it is clear that the open boundary condition can be regarded as a special case of the irradiation situation. Energy is now irradiated from the computational domain to the exterior. Therefore, the condition (4.17a) for the covering of the fictitious grid cells C_R can be taken, yielding for the TE fields

$$E_{1,R} = E_{1,L}, \qquad E_{2,R} = E_{2,L}, \qquad B_{3,R} = B_{3,L}. \tag{4.19a}$$

Using once again the result (4.18), we obtain from (4.17b) the instruction how to cover the dummy cells C_R for the correction

$$\Phi_R = 2\Phi_0 - \Phi_L, \tag{4.19b}$$

where for the value at the border Φ_0 the approximate result (4.14) can be used.

5. NUMERICAL RESULTS

The Maxwell solver with purely hyperbolic correction is applied in two different situations. First, simulation results of a pure electromagnetic field problem are presented. Second, an electromagnetic PIC calculation is discussed, where the FV Maxwell solver is used as one part in a simulation program which solves numerically the Maxwell–Vlasov equations.

5.1. Application to a pure electromagnetic field problem. Let us consider a simple two-dimensional field problem without any symmetry for which Cartesian coordinates $\boldsymbol{x} = (x_1, x_2) = (x, y)$ are suitable. It is easy to check that the TE field components

$$\begin{aligned} E_1(x, y, t) &= -\frac{k_\perp}{k_\parallel} \sin(k_\perp y) \cos(k_\parallel x - \omega t), \\ E_2(x, y, t) &= \cos(k_\perp y) \sin(k_\parallel x - \omega t), \\ B_3(x, y, t) &= \frac{\omega}{k_\parallel c^2} \cos(k_\perp y) \sin(k_\parallel x - \omega t), \end{aligned} \tag{5.1a}$$

are a set of solutions of the time-dependent Maxwell equations (2.1a) and (2.1b) for which the divergence condition $\nabla \cdot \boldsymbol{E} = 0$ holds. The longitudinal and transverse wave numbers $k_\parallel$ and $k_\perp$, respectively, are related to the frequency ω according to

$$k_\parallel^2 + k_\perp^2 = \frac{\omega^2}{c^2}. \tag{5.1b}$$

The numerical experiments are performed on the domain $\Omega = [0, 1] \times [0, 1]$ which consists of a unit square with an edge length of 1 m. The discretization of this computational domain is established by a structured mesh of 20×20 non-orthogonal grid zones as depicted in Fig. 4. Additionally, a refined grid of 40×40 mesh zones will be used. In order to check simultaneously different kinds of boundary conditions, we limit the computational domain

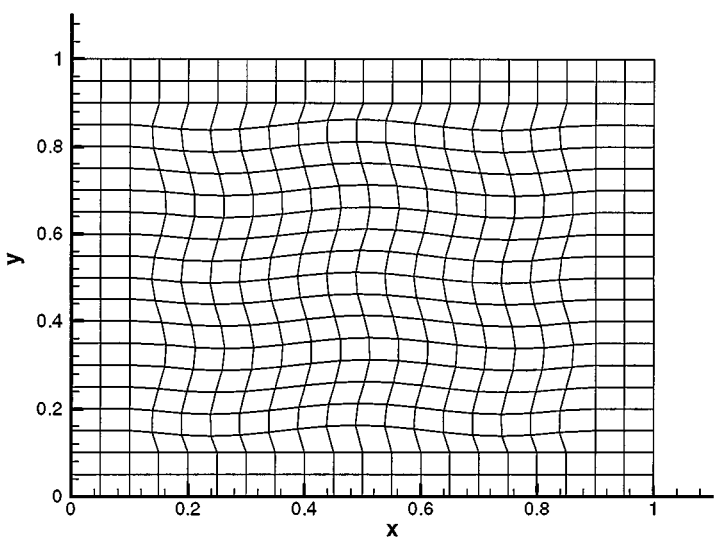

FIG. 4. Discretization of the computational domain by a structured mesh of 20×20 non-orthogonal grid zones.

at $y = 0$ and $y = 1$ m by a perfectly conducting wall. This means that the transverse electrical field of the TE system vanishes there,

$$E_1(x, 0, t) = E_1(x, 1, t) = 0, \qquad \forall (x, t). \tag{5.1c}$$

This leads to the requirement that the transverse wave number has to be chosen according to

$$k_\perp = p\pi, \qquad p \in \mathbb{Z}. \tag{5.1d}$$

Furthermore, we prescribe irradiation of electromagnetic energy at $x = 0$ given by the analytical values of (5.1a) at that boundary and truncate the computational domain artificially at $x = 1$ m. Performing numerical experiments, we choose $k_\parallel = k_\perp = \pi$ (measured per meter) and initialize the TE fields according to the analytical solution (5.1a) at time $t = 0$. An overview of the numerical solution on the truncated computational domain for the initial-boundary problem (5.1) is given in Fig. 5. There, the temporal evolution of the

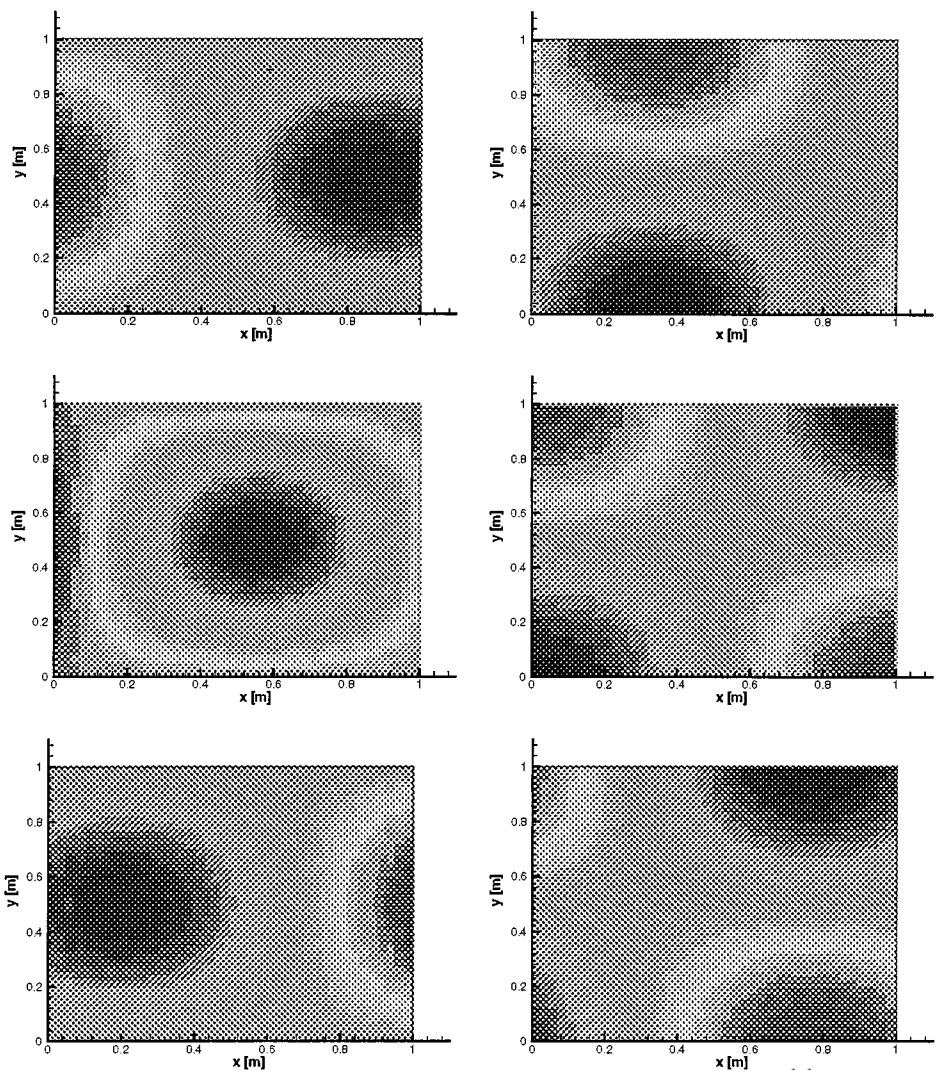

FIG. 5. Three snapshots of the E_1 (left) and E_2 (right) field component recorded at $t = 2$, $t = 6$, and $t = 10$ ns. These numerical results are computed without any correction.

E_1 component (left) and E_2 component (right) of the TE system is depicted at the times $t = 2$, $t = 6$, and $t = 10$ ns, corresponding to 100, 300, and 500 iteration cycles, respectively. The three (uncorrected and via the elliptic or hyperbolic approach corrected) second-order accurate Maxwell solver implementations produce almost the same numerical results for the pure field calculation compared to the analytical solution. This again illustrates that for pure field calculations, the divergence errors do not dramatically influence the solution. However, differences in the divergence constraint approximation for the three methods can be seen. For that, we define the divergence of a vector field $\boldsymbol{F}(\boldsymbol{x}, t)$ at $t = t^n$ for the grid zone C_i in a FV sense according to

$$[\nabla \cdot \boldsymbol{F}]_i^n := \frac{1}{V_i} \int_{C_i} \nabla \cdot \boldsymbol{F}(\boldsymbol{x}, t^n)\, dV \approx \frac{1}{2V_i} \sum_{\beta=1}^{\sigma_i} L_{i,\beta} \left(\boldsymbol{F}_i^n + \boldsymbol{F}_{i_\beta}^n\right) \cdot \boldsymbol{n}_{i,\beta}. \tag{5.2}$$

Its discrete L_2-error norm at the time $t = t^n$ given by

$$\|\nabla \cdot \boldsymbol{F}(\boldsymbol{x}, t^n)\|_{L_2} = \sqrt{\sum_{i=1}^{N} \left|[\nabla \cdot \boldsymbol{F}]_i^n\right|^2 V_i} \tag{5.3}$$

is an appropriate and evident measure to check the quality of the divergence approximation. To get a quantitative picture, we compute this discrete L_2-error norm of $\nabla \cdot \boldsymbol{E}$ for two different computational meshes (20×20 and 40×40 grid zones). The numerical results are presented in Fig. 6, where $\|\nabla \cdot \boldsymbol{E}(\boldsymbol{x}, t)\|_{L_2}$ is plotted versus time for the uncorrected (upper), the elliptic (middle), and the purely hyperbolic (lower picture) correction approach. There, we observe that the time monitored L_2 error for the 20×20 grid calculated with the schemes where a correction is applied lies significantly below those computed with the uncorrected Maxwell solver. When the computational grid is refined, the error in the corrected cases decreases in an expected manner, while in the uncorrected case no improvement is obtained. A direct comparison of the numerical results computed with the three different field solvers for the 40×40 grid is seen in Fig. 7. The temporal evolution of the L_2-error of $\nabla \cdot \boldsymbol{E}$ drops by more than a factor of four using a corrected (open circles, solid triangles) instead of the uncorrected (solid squares) FV scheme. The hyperbolic correction approach yields approximations nearly as accurate as the standard Boris method based on the numerical solution of an elliptic Poisson equation with less computational effort.

5.2. Application in an electromagnetic PIC simulation. In the following we simulate a typical situation occurring in the field of electromagnetic PIC applications where the Maxwell solver is one part of a complex simulation program. Due to the numerical approximation of the particle motion and the calculation of the charge density from the particle distribution, charge errors will occur in this situation. We consider a radiating magnetic dipole in the xy-plane (see Fig. 8) modeled by 36 negative charged macro particles revolving due to an externally applied static magnetic induction $B_3^{ext} = 0.25$ Vs/m^2 on a circle with a radius of $r_0 = 0.18$ cm centered at $(x_0, y_0) = (49.5$ cm, 49.5 cm). Each macro particle carries a charge of $Q = -10^{-10}$ As (equivalent to $6.24 \cdot 10^8$ electrons as constituents) and possesses an initial velocity of $v_0 = 7.49 \cdot 10^7$ m/s tangential to the trajectory. This artificially high velocity was chosen to minimize space-charge effects in the circular current loop. The numerical experiments are performed for a square with an edge length of 1 m, discretized by a Cartesian mesh of 100×100 grid zones. Open boundary conditions

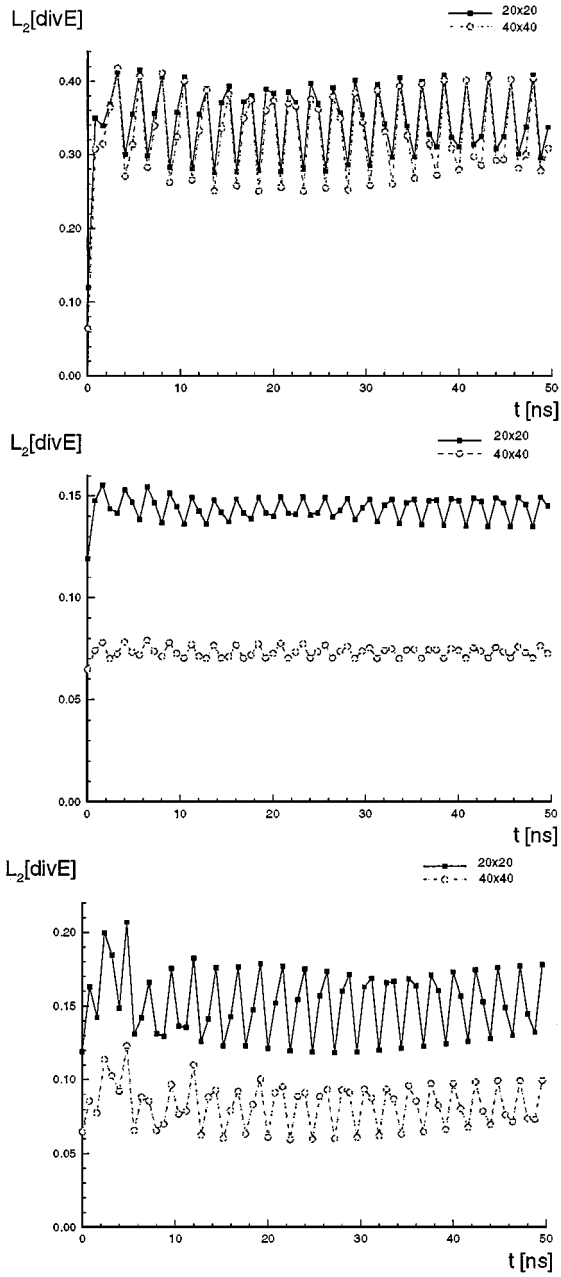

FIG. 6. Temporal behavior of the discrete L_2-error norm computed according to Eq. (5.3) for the uncorrected scheme (upper plot) as well as for the cases where the elliptical (middle) and purely hyperbolic (lower plot) correction approaches are applied. The computations are performed on the mesh depicted in Fig. 4 and a further refinement.

are prescribed at the four borders of the computational domain, while truncated domain conditions (cf. Subsection 4.4.4) have to be imposed on the boundaries for the hyperbolic correction function Φ.

As for the situation where the eigenfields of the moving charges are neglected, we expect as a consequence of the special choice of the physical parameters that a circular trajectory

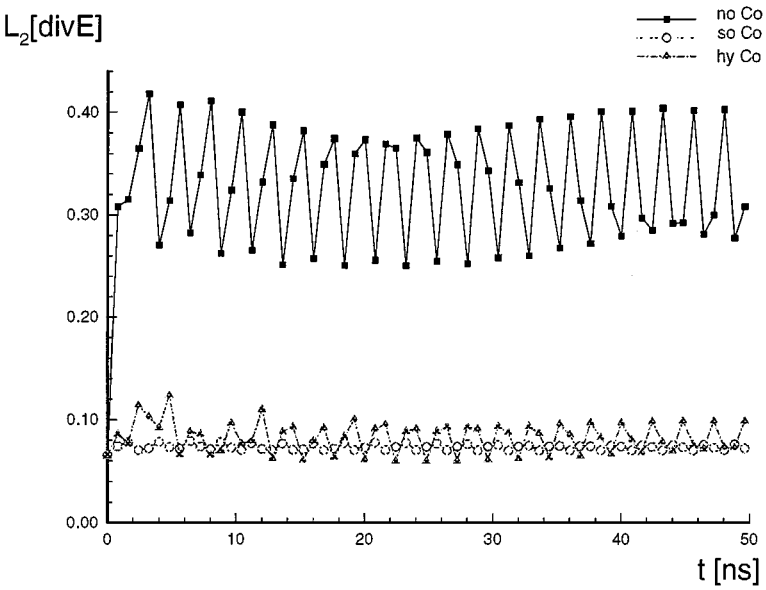

FIG. 7. Comparison of the discrete L_2-error norm computed with the uncorrected (solid squares), elliptical (open circles), and hyperbolical (solid triangles) corrected Maxwell solver implementation for the 40×40 computational grid.

is retained for a sufficient long period of time, even here, where the fields are calculated in a self-consistent manner. This conjecture is confirmed in Fig. 8, where the actual locations of the macro particles are seen at time $t = 7$ ns. Obviously, after 47.4 revolutions of each charge the ensemble of particles are on a circle which is centered at the intersection of four adjacent grid zones. We stress, however, that in general no exact solution is available for this model

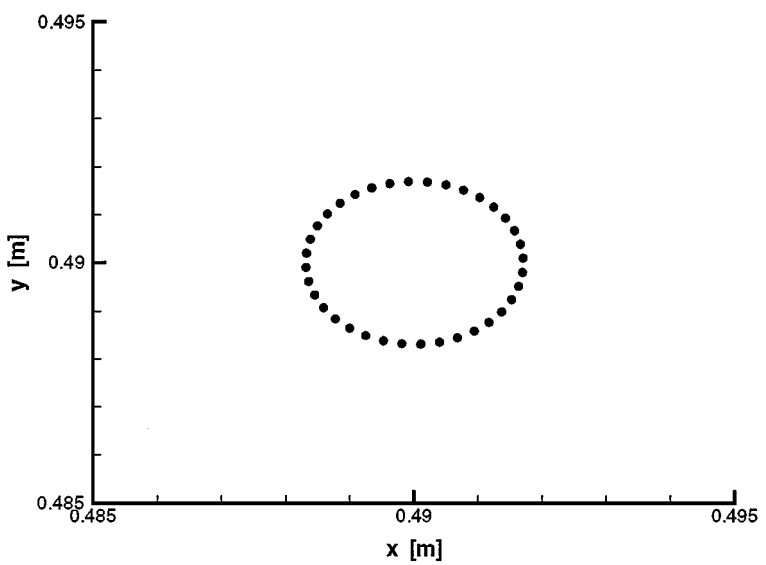

FIG. 8. Numerical model of a magnetic dipole in the xy-plane. The snapshot at $t = 7$ ns shows the location of the 36 negative-charged macro particles moving due to an externally applied magnetic induction on a circle with a diameter of approximately 0.36 cm.

problem: Especially, when the charge of the particles is further increased, eigenfields are substantial and self-consistent field-particle computations are imperative. Therefore, in the following we compare numerical results obtained with an electromagnetic PIC simulation program where three different Maxwell solver are available. Numerical simulations with the uncorrected as well as the elliptical and the purely hyperbolic Maxwell solver are performed, where both correction techniques are incorporated into the scheme by applying a splitting approach. The elliptic correction uses a combined ad hoc SOR and Jacobi scheme to solve the Poisson equation (3.1b) on non-uniform grids [35] and is applied during the calculation after each fifth temporal iteration cycle. In contrast, the hyperbolic correction is computed at each time step, where we choose a value of one for the parameter χ (cf. Subsection 3.3) and fix α (cf. Subsection 4.4) equal to the reflection case, that is, $\alpha = -1$.

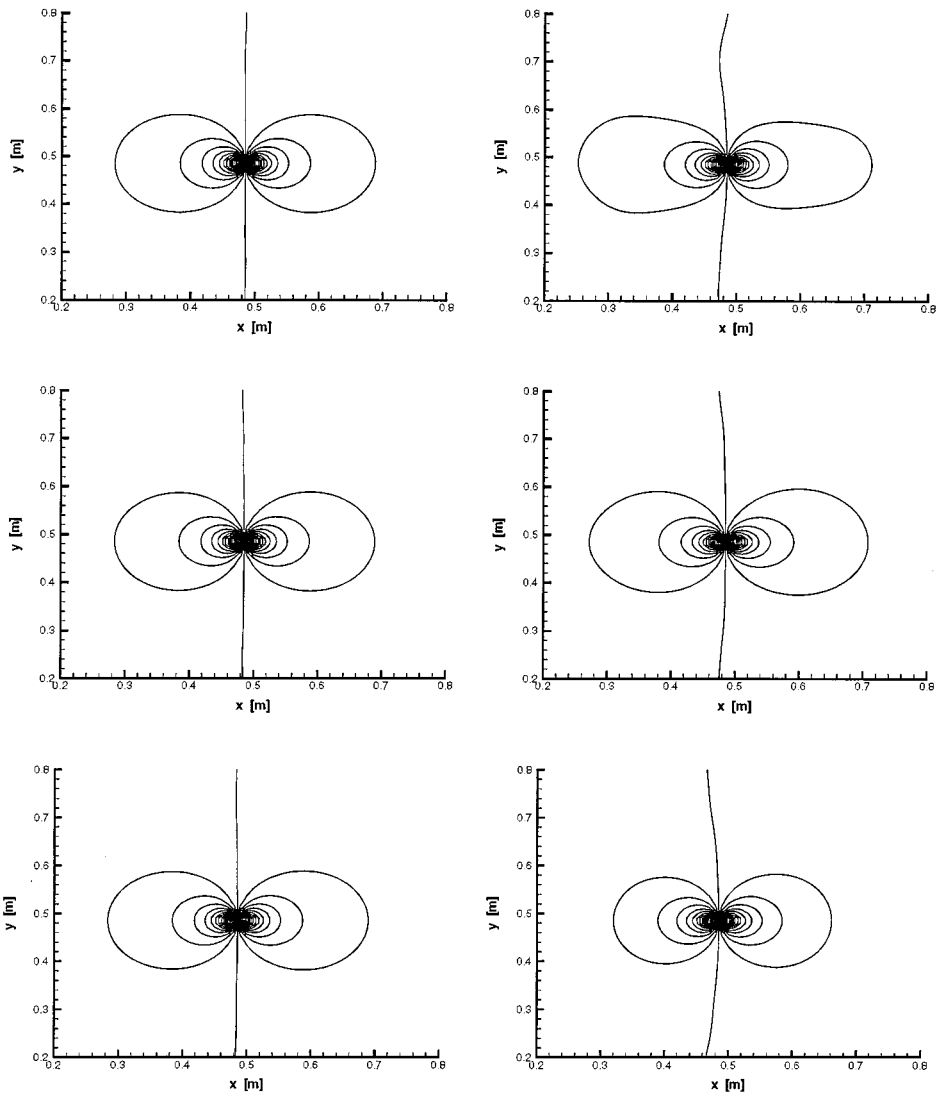

FIG. 9. Three snapshots of the E_1 field component of the magnetic dipole recorded at $t = 1$, $t = 3$, and $t = 5$ ns. The PIC approximation errors are corrected by using an elliptic (left column) and a purely hyperbolic (right column) Maxwell solver implementation.

A first simulation result of the self-consistent field formation of a magnetic dipole in the xy-plane has already been presented in Fig. 1. There, the E_2 field is computed with an uncorrected (left) and elliptic correction-based (right) Maxwell solver and recorded at the times $t = 1$, $t = 3$, and $t = 5$ ns corresponding to 220, 660, and 1100 iteration cycles, respectively. Inspecting the central contour lines of the left plot sequence, we clearly recognize that the uncorrected field solution runs into a highly unphysical regime. The right sequence of results shows the numerical solution obtained for the dipole simulation where the elliptic correction technique is applied after the conventional Maxwell solver. These are the well-known contour shapes for the far-field of a magnetic dipole. In Fig. 9, a direct comparison between the E_1 magnetic dipole field distribution calculated with the elliptic (left) and purely hyperbolic (right) Maxwell solver is given for three different times ($t = 1$, $t = 3$, and $t = 5$). These plots clearly reveal that the global features as well as the detailed structure of the field distribution computed with the purely hyperbolic correction technique is in excellent agreement with those obtained from the standard elliptic correction approach. The comparison of the temporal evolution of the discrete L_2-norm of $\nabla \cdot \boldsymbol{E} - \rho/\epsilon_0$ determined from Eq. (5.3) is seen for the implementations under discussion in Fig. 10. It is clearly visible that the L_2-error norm computed with the conventional uncorrected Maxwell solver increases with respect to time, indicating that the corresponding numerical solution of the Maxwell–Vlasov equations becomes unphysical. Furthermore, we conclude from Fig. 10 that the PIC simulation program equipped with an elliptic as well as purely hyperbolic Maxwell solver yields a nearly constant discrete L_2-error norm of $\nabla \cdot \boldsymbol{E} - \rho/\epsilon_0$ in the course of the numerical experiment. Additionally, the result computed with the hyperbolic correction approach even lies below the one obtained with the standard elliptic correction technique. Depending on how often the elliptic correction is performed, cost might be comparable on regular grids. However, elliptic solvers become more expensive on unstructured

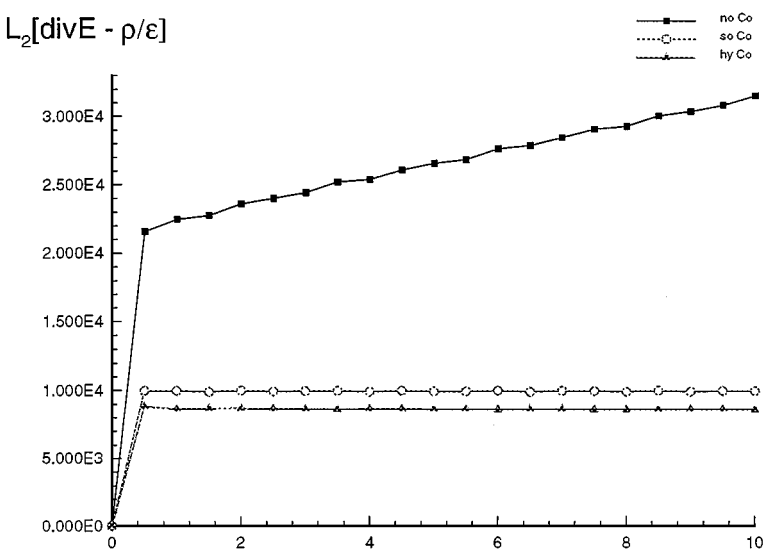

FIG. 10. Comparison of the temporal behavior of the discrete L_2-error norm of $\nabla \cdot \boldsymbol{E} - \rho/\epsilon_0$ computed according to Eq. (5.3) for three Maxwell solver implementations. The plotted results are obtained with the uncorrected (solid squares), elliptical (open circles), and hyperbolical (solid triangles) corrected Maxwell solver for a 100×100 Cartesian mesh.

grids and on parallel computers. Notice also that the purely hyperbolic formulation is the only one of the GLM formulations which is fully relativistic like the original Maxwell equations.

6. CONCLUSIONAL REMARKS

Numerical methods for the Maxwell equations are usually based on the hyperbolic evolution equations for the electromagnetic fields $\boldsymbol{E}$ and $\boldsymbol{B}$ only, where the current density enters as source. As a consequence, one observes that the elliptic divergence constraints of the Maxwell system are only satisfied approximately. Especially in the context of electromagnetic PIC calculations where charge conservation errors occur, the consistency with charge density is lost. Consequently, small errors may dramatically accumulate during the simulation, generating wrong and unphysical numerical solutions. Hence, in those cases a suitable numerical scheme has to take care to ensure that these divergence errors do not increase in the course of time and that the consistency of $\nabla \cdot \boldsymbol{E}$ with the charge density is guaranteed. To do this, we propose in this paper a scheme enforcing the divergence equations of the Maxwell system by directly incorporating these conditions into the numerical approximation. For that, we introduce the new generalized Lagrange multiplier (GLM) formulation of the Maxwell equations which is a mathematical model allowing errors in the divergence constraints and charge conservation and which yields approximate solutions of the conventional Maxwell equations. In the present discussions, we restricted ourselves to the situation where the charge conservation is erroneous, resulting in a coupled system of the time-dependent Maxwell equations and Gauss' law which is satisfied approximately during the temporal evolution.

The proposed GLM formulation recovers the well-known charge correction technique of Boris [4] and also the parabolic approach of Marder [24]. The purely hyperbolic correction technique, however, is an interesting alternative approximation method for the charge conservation constraint and fits in an excellent manner into the environment of explicit field computations based on high-resolution finite-volume schemes. Especially, this hyperbolic correction ansatz is very flexible and efficient for code implementation and code running on computers with parallel architecture. Furthermore, our simulation results obtained for a pure field computation as well as an electromagnetic PIC calculation clearly reveal that the hyperbolic correction approach yields approximations nearly as accurate as the standard technique which solves an elliptic Poisson equation with less computational effort. And last but not least, the hyperbolic formulation retains the relativistic form of the original Maxwell equations.

ACKNOWLEDGMENTS

The authors acknowledge the reviewers for the critical review of the manuscript, the useful comments, and the helpful suggestions, which we have taken into account.

REFERENCES

1. J. J. Ambrosiano, S. T. Brandon, R. Löhner, and C. DeVore, Electromagnetics via the Taylor–Galerkin finite element method on unstructured grids, *J. Comput. Phys.* **110**, 310 (1994).
2. F. Assous, P. Degond, E. Heintze, P. Raviart, and J. Segré, On a finite-element method for solving the three-dimensional Maxwell equations, *J. Comput. Phys.* **109**, 222 (1993).

3. C. K. Birdsall and A. B. Langdon, *Plasma Physics via Computer Simulation* (McGraw–Hill, New York, 1985).
4. J. P. Boris, Relativistic plasma simulations—Optimization of a hybrid code, in *Proc. 4th Conf. on Num. Sim. of Plasmas, NRL Washington, Washington DC, 1970*, p. 3.
5. J. P. Cioni, L. Fezoui, and H. Steve, A parallel time-domain Maxwell solver using upwind schemes and triangular meshes, *IMPACT Comput. Sci. Eng.* **5**, 215 (1993).
6. E. Courant, E. Isaacson, and M. Rees, On the solution of nonlinear hyperbolic differential equations, *Comm. Pure Appl. Math.* **5**, 243 (1953).
7. L. Durlofsky, B. Engquist, and S. Osher, Triangle based adaptive stencils for the solution of hyperbolic conservation laws, *J. Comput. Phys.* **98**, 64 (1992).
8. J. W. Eastwood, The virtual particle electromagnetic particle-mesh method, *Comput. Phys. Comm.* **64**, 252 (1991).
9. M. Fedoruk, C.-D. Munz, P. Omnes, and R. Schneider, *A Maxwell–Lorentz Solver for Self-Consistent Particle-Field Simulations on Unstructured Grids*, Forschungszentrum Karlsruhe—Technik und Umwelt, FZKA 6115, 1998.
10. S. K. Godunov, Finite difference method for numerical computation of discontinuous solutions of the equations of fluid dynamics, *Mat. Sb.* **47**, 271 (1959).
11. E. Halter, M. Krauss, C.-D. Munz, R. Schneider, E. Stein, U. Voss, and T. Westermann, *A Concept for the Numerical Solution of the Maxwell–Vlasov System*, Forschungszentrum Karlsruhe—Technik und Umwelt, FZKA 5654, 1995.
12. G. W. Hedstrom, Non-reflecting boundary conditions for nonlinear hyperbolic systems, *J. Comput. Phys.* **30**, 222 (1979).
13. R. W. Hockney and J. W. Eastwood, *Computer Simulation Using Particles* (McGraw–Hill, New York, 1981).
14. R. Holland, Finite-difference solution of Maxwell's equations in generalized nonorthogonal coordinates, *IEEE Trans. Nucl. Sci.* **30**, 4589 (1983).
15. J. M. Hyman and M. Y. Shashkov, Natural discretizations for the divergence, gradient, and curl on logically rectangular grids, *Comput. Math. Appl.* **33**, 81 (1997).
16. B. Jiang, *The Least-Squares Finite Element Method, Theory and Applications in Computational Fluid Dynamics and Electromagnetics* (Springer-Verlag, Heidelberg, 1998).
17. B. Jiang, J. Wu, and L. A. Povinelli, The origin of spurious solutions in computational electromagnetics, *J. Comput. Phys.* **125**, 104 (1996).
18. V. Komornik and E. Zuazua, A direct method for the boundary stabilization of the wave equation, *J. Math. Pures Appl.* **69**, 33 (1990).
19. A. B. Langdon, On enforcing Gauss' law in electromagnetic particle-in-cell codes, *Comput. Phys. Comm.* **70**, 447 (1992).
20. B. v. Leer, Towards the ultimative conservative difference scheme. V. A second order sequel to Godunov's method, *J. Comput. Phys.* **32**, 101 (1979).
21. R. J. LeVeque, *Numerical Methods for Conservation Laws* (Birkhäuser, Basel, 1990).
22. N. K. Madsen and R. W. Ziolkowski, A three-dimensional modified finite volume technique for Maxwell's equations, *Electromagnetics* **10**, 147 (1990).
23. G. Marchuk, *Methods of Numerical Mathematics* (Springer-Verlag, New York/Heidelberg/Berlin, 1975).
24. B. Marder, A method incorporating Gauß' law into electromagnetic PIC codes, *J. Comput. Phys.* **68**, 48 (1987).
25. R. L. Morse and C. W. Nielson, Numerical simulation of the Weibel instability in one and two dimensions, *Phys. Fluids* **14**, 830 (1971).
26. C.-D. Munz, R. Schneider, E. Sonnendrücker, E. Stein, U. Voss, and T. Westermann, A finite-volume particle-in-cell method for the numerical treatment of the Maxwell–Lorentz equations on boundary-fitted meshes, *Int. J. Numer. Meth. Eng.* **44**, 461 (1999).
27. C.-D. Munz, R. Schneider, E. Sonnendrücker, and U. Voss, Maxwell's equations when the charge conservation is not satisfied, *C. R. Acad. Sci. Paris* **328**, 431 (1999).
28. C.-D. Munz, R. Schneider, and U. Voss, A finite-volume method for Maxwell equations in time domain, *SIAM J. Sci. Comput.*, in press.

29. D. E. Nielsen and A. T. Drobot, An analysis of the pseudo-current method, *J. Comput. Phys.* **89**, 31 (1990).
30. W. Schwalm, B. Moritz, M. Giona, and M. Schwalm, Vector difference calculus for physical lattice models, *Phys. Rev. E* **59**, 1217 (1999).
31. G. Strang, On the construction and comparison of difference schemes, *SIAM J. Numer. Anal.* **5**, 505 (1968).
32. F. L. Teixeira and W. C. Chew, Lattice electromagnetic theory from a topological viewpoint, *J. Math. Phys.* **40**, 169 (1999).
33. J. Villasenor and O. Buneman, Rigorous charge conservation for local electromagnetic field solvers, *Comput. Phys. Comm.* **69**, 306 (1992).
34. T. Westermann, Localization schemes in 2D boundary-fitted grids, *J. Comput. Phys.* **101**, 307 (1992).
35. T. Westermann, Numerical modelling of the stationary Maxwell–Lorentz system in technical devices, *Int. J. Numer. Mod.* **7**, 43 (1994).
36. K. S. Yee, Numerical solution of initial boundary value problems involving Maxwell's equations in isotropic media, *IEEE Trans. Antennas Propag.* **14**, 302 (1966).